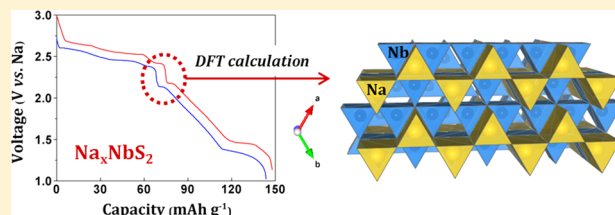


Sodium Intercalation Behavior of Layered  $\text{Na}_x\text{NbS}_2$  ( $0 \leq x \leq 1$ )Youhao Liao,<sup>†,‡,||</sup> Kyu-Sung Park,<sup>‡,||</sup> Penghao Xiao,<sup>§</sup> Graeme Henkelman,<sup>‡,§</sup> Weishan Li,<sup>†</sup>  
and John B. Goodenough<sup>‡,\*</sup><sup>†</sup>School of Chemistry and Environment, South China Normal University, Guangzhou, 510006, P.R. China<sup>‡</sup>Texas Materials Institute and Materials Science and Engineering Program and <sup>§</sup>Department of Chemistry, University of Texas at Austin, Austin, Texas 78712, United States

## Supporting Information

**ABSTRACT:** A layered sulfide,  $\text{Na}_{0.5}\text{NbS}_2$  (space group:  $P6_3/mmc$ ), was synthesized by a conventional solid-state reaction as an electrode material for a Na-ion battery. Galvanostatic Na insertion/extraction was performed to characterize the system  $\text{Na}_x\text{NbS}_2$  ( $0 \leq x \leq 1.0$ ) operating on the Nb(IV)/Nb(III) redox couple. Although the system shows a high specific capacity of  $143.6 \text{ mAh g}^{-1}$ , the voltage profile is not suitable with a signature of Na/vacancy ordering at  $x = 0.5$ . First-principles calculation was applied to reveal possible structures of  $\text{Na}_x\text{NbS}_2$  and describe the corresponding electrochemical properties. The calculated Na binding energies and voltages are in good agreement with experimental charge/discharge voltages. We also found a possible atomic arrangement of Na/vacancy ordering in  $\text{Na}_{0.5}\text{NbS}_2$ . Although layered  $\text{NaMS}_2$  systems allow full sodium intercalation, the strong  $\text{Na}^+ - \text{Na}^+$  intralayer interaction induces layer gliding and  $\text{Na}^+$ -ion ordering that create undesirable steps in the voltage profile.

**KEYWORDS:**  $\text{Na}_x\text{NbS}_2$ , Na/vacancy ordering, sodium ion battery



## 1. INTRODUCTION

In the past decades, the rechargeable lithium-ion battery has been an important power source for portable electronics and is also starting to power hybrid electric vehicles. However, besides its high price, the limited and localized lithium resource will be an obstacle to expand its application to energy storage in the kWh to MWh scale.<sup>1</sup> The sodium-ion battery provides an interesting alternative because it can directly adopt the rich chemistry and the state-of-the-art engineering developments of the lithium-ion battery. For example,  $\text{NaCoO}_2$ ,  $\text{NaFe}_{0.5}\text{Mn}_{0.5}\text{O}_2$ ,  $\text{NaNi}_{0.5}\text{Mn}_{0.5}\text{O}_2$ ,  $\text{NaCrO}_2$ ,  $\text{NaVO}_2$ ,  $\text{NaFePO}_4$ , and  $\text{Na}_3\text{V}_2(\text{PO}_4)_3$  can be found in recent publications.<sup>2–8</sup> However, we have yet to determine whether a layered transition-metal compound can be a viable option for a Na-ion battery as it is in a Li-ion battery.

In this work, we examine a layered transition-metal disulfide that is believed to be a better Na-intercalation host than the layered oxides and we investigate the  $\text{Na}^+ - \text{Na}^+$  Coulombic interactions in a layered compound. Niobium disulfide,  $\text{NbS}_2$ , has a hexagonal structure with Nb atoms in a trigonal-prismatic sulfur site; the  $\text{NbS}_2$  sandwich layers are weakly bound together by van der Waals forces.<sup>9</sup> Within the Nb slabs,  $\text{NbS}_6$  trigonal prisms share edges with six nearest  $\text{NbS}_6$  neighbors, and the interslab space consists of edge-shared octahedral sites. Chemically synthesized  $\text{Na}_x\text{NbS}_2$  ( $0.4 \leq x \leq 1.0$ ) was reported by Omloo and Jellinek in 1970; it showed Na in the gallery space between the  $\text{NbS}_2$  layers.<sup>10</sup> However, once Na intercalates into the structure, it causes a gliding of the  $\text{NbS}_2$  slabs to create trigonal-prismatic sites in the gallery space.<sup>11</sup> In

$\text{NbS}_2$ , Nb atoms have the same  $(x, y)$  positions along the  $z$ -axis in the hexagonal unit cell, but in  $\text{Na}_{0.5}\text{NbS}_2$ , in contrast, S atoms have the same  $(x, y)$  positions while keeping the  $\text{NbS}_6$  prismatic structure. Since the slabs are bound weakly by van der Waals forces, layer sliding should not cost too much energy. However, the intercalated Na ions have strong Coulombic interactions between themselves. To our knowledge, there are no previous reports of Na-ion battery performance of  $\text{Na}_x\text{NbS}_2$  ( $0 \leq x \leq 1.0$ ) that reflects Na binding energy to the host structure, which is important to understand its intercalation chemistry.

Electrochemical methods are useful to isolate compounds that are not easily prepared by synthetic chemistry. Recently,  $\text{Na}_{2/3}\text{CoO}_2$  and  $\text{Na}_{1/2}\text{CoO}_2$  have been successfully isolated by applying specific voltages during the electrochemical study on  $\text{P2-Na}_x\text{CoO}_2$  ( $x \leq 1$ ).<sup>2</sup> In this regard, electrochemical characterization of  $\text{Na}_{0.5}\text{NbS}_2$ , which is easily made by a solid state reaction, can be used to give information about the  $\text{Na}_x\text{NbS}_2$  ( $0 \leq x \leq 1.0$ ) materials. In addition to electrochemical and structural characterizations, density functional theory (DFT) calculations are also used to find the most stable atomic configuration in each composition. X-ray structural analysis is limited in this case because the layered disulfide structure brings very strong preferred orientation, which makes it difficult to refine the atomic positions. The DFT calculations are particularly useful to clarify the Na insertion process, which

Received: January 14, 2013

Revised: March 7, 2013

Published: March 28, 2013

is accompanied by Na order/disorder transitions as well as by interlayer glide. Additionally, the charge/discharge cycle performance of  $\text{Na}_x\text{NbS}_2$  at different current densities is presented for the first time.

## 2. EXPERIMENTAL AND THEORETICAL METHODS

A series of  $\text{Na}_x\text{NbS}_2$  ( $0.0 \leq x \leq 1.0$ ) materials were synthesized by a conventional solid-state reaction of  $\text{Na}_2\text{S}$  (Alfa Aesar, 99.9%; with 3 wt % excess to compensate for the loss of sodium during annealing for  $x \geq 0.7$  in  $\text{Na}_x\text{NbS}_2$ ) with Nb (Alfa Aesar, 99.95%) and S (Alfa Aesar, 99.5%). The powder mixture was ground in a mortar for 1 h, pressed into a pellet, and then put into a quartz tube. The tube was pre-dried and carbon-coated before use. All the steps were finished in an Ar-filled glovebox. After taking the tube out of the glovebox, it was evacuated and sealed with a flame. The samples were heated slowly to 700 °C for 20 h and kept at that temperature for 15 h, and then cooled slowly to 250 °C for 35 h followed by quenching to room temperature. The final (gray) samples were removed from the tubes and ground in the glovebox for further characterization.

X-ray diffraction (XRD, Cu  $K\alpha$  source with 40 kV and 30 mA; PANalytical X'Pert Pro MPD) was used to detect the phase formation and calculate the lattice parameters of the powder samples. The materials for XRD measurement were prepared by charging/discharging an electrochemical cathode to a designed voltage followed by constant-voltage duration until the current became below 1  $\mu\text{A}$ . The XRD patterns were recorded in the  $2\theta$  range from 10° to 90° with a step width of 0.03° and a dwell time of 5 s at room temperature. An XRD sample was put into a sample holder with a cover of thin, amorphous polyimide film in the glovebox to avoid contact with moisture and oxygen. The FullProf software was used to obtain lattice parameters without consideration of atomic positions.

$\text{Na}_{0.5}\text{NbS}_2$  was chosen to test the electrochemical performance of  $\text{Na}_x\text{NbS}_2$  ( $0 \leq x \leq 1.0$ ). A composite electrode was obtained by mixing 75 wt % of  $\text{Na}_{0.5}\text{NbS}_2$  powder with 20 wt % of acetylene black as a conductive agent and 5 wt % of polytetrafluoroethylene (PTFE) as a binder in the glovebox. Standard 2032-type Na/ $\text{Na}_{0.5}\text{NbS}_2$  coin cells were assembled, and charge/discharge tests were carried out with a Land Battery Test System (Wuhan Land Electronic Co. Ltd.). The electrolyte composition was 1 M  $\text{NaPF}_6$  in ethylene carbonate (EC) and diethyl carbonate (DEC) (1:1 in volume).

Calculations of the material energies were done with density functional theory (DFT) at the general gradient approximation (GGA) level of theory with the PW91 functional as implemented in the Vienna ab initio simulation package.<sup>12–14</sup> No spin polarization was applied with metallic 4d electrons because several tests showed that the ground-state structures had spin-paired electrons.

In order to find the lowest energy structure(s) for a given Na composition, the basin-hopping algorithm was used with Na-vacancy swapping moves.<sup>15</sup> The local minimization part of the basin-hopping algorithm was done with a reduced accuracy, specifically, with a single  $k$ -point, a plane-wave energy cutoff of 260 eV to represent the valence electrons, and a loose convergence criterion for the geometry of a maximum of 0.1 eV/Å for any atom. This procedure allowed for the exploration of hundreds of local minima at each Na concentration. For the global minima, formation energies were recalculated with stricter settings, i.e. with geometries converged to 0.01 eV/Å, a higher  $2 \times 2 \times 2$   $k$ -point mesh, and a higher energy cutoff of 340 eV. Lattice parameters are relaxed in all the calculations.

## 3. RESULTS AND DISCUSSION

It is reported that lithium can intercalate into the layered  $\text{NbS}_2$  up to one Li per formula unit.<sup>16</sup> The half-cell voltage curve of  $\text{Li}_x\text{NbS}_2$  ( $0 \leq x \leq 1$ ) shows solid-solution characteristics, which indicates no Li ordering or structural changes during Li insertion/extraction. However, Na insertion into the  $\text{NbS}_2$  host exhibits a different intercalation behavior. Figure 1 shows the galvanostatic charge/discharge voltage curves of  $\text{Na}_x\text{NbS}_2$  ( $0 \leq x \leq 1$ ) at the rate of  $C/20$ . It shows a specific discharge capacity

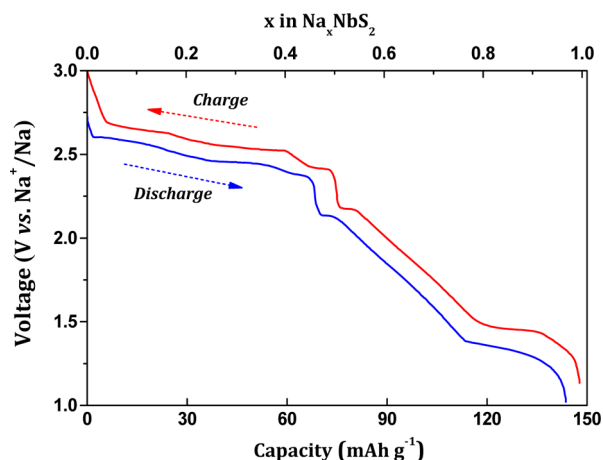


**Figure 1.** Galvanostatic charge/discharge voltage curves of  $\text{Na}_x\text{NbS}_2$  in the voltage range of 1.0–3.0 V at  $C/20$ -rate.

of 143.6  $\text{mAh g}^{-1}$ , which is close to the theoretical capacity of  $\text{NaNbS}_2$ , 148.9  $\text{mAh g}^{-1}$ , calculated based on the Nb(IV)/Nb(III) redox couple. A distinctive drop in the voltage curve could be seen at  $\text{Na}_{0.5}\text{NbS}_2$ . The 0.5 Na composition separates relatively stable voltages in  $0 \leq x \leq 0.5$  (2.35–2.6 V vs Na) and linearly decreasing voltages in  $0.5 \leq x \leq 0.75$ . A similar Na intercalation behavior could also be found in other layered Na-intercalation compounds like  $\text{NaCoO}_2$  and  $\text{NaVO}_2$ .<sup>2,6</sup> The data suggest that  $\text{Na}_{0.5}\text{NbS}_2$  (space group:  $P6_3/mmc$ ) has a Na/vacancy ordering because the voltage drop at 0.5 Na shows that an atomic structure of this specific composition is very stable. We adopt DFT calculations to find a possible Na/vacancy ordered structure; it is discussed in the following computation section. In addition to the Na/vacancy ordering behavior, *ex situ* electrode X-ray diffraction and powder X-ray diffraction for  $\text{Na}_x\text{NbS}_2$  ( $0 \leq x \leq 1$ ) were performed to clarify the electrochemistry of  $\text{Na}_x\text{NbS}_2$ .

To check whether the structure of the electrode material is changed during the Na intercalation process, we disassembled the coin cells of  $x = 0$  ( $\text{NbS}_2$ , charge to 3.0 V) and  $x = 1$  ( $\text{NaNbS}_2$ , discharge to 1.0 V) compositions. Figure 2 shows the

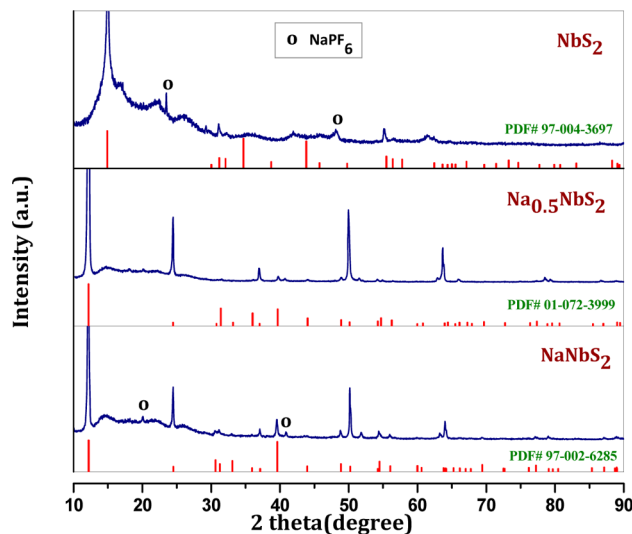


**Figure 2.** XRD patterns of the pristine  $\text{Na}_{0.5}\text{NbS}_2$  electrode,  $\text{NbS}_2$  electrode (charged to 3.0 V), and  $\text{NaNbS}_2$  electrode (discharged to 1 V).

electrode XRD patterns of  $\text{Na}_{0.5}\text{NbS}_2$ ,  $\text{NbS}_2$ , and  $\text{NaNbS}_2$  electrodes. The main diffraction peaks are in accordance with the standard cards of  $\text{Na}_{0.5}\text{NbS}_2$  (PDF no. 01-072-3999, space group:  $P6_3/mmc$ ),  $\text{NbS}_2$  (PDF no. 97-004-3697,  $P6_3/mmc$ ), and  $\text{NaNbS}_2$  (PDF no. 97-002-6285,  $P6_3/mmc$ ) except for the residual sodium salt,  $\text{NaPF}_6$ . However, the relative intensity ratio deviates from the standard card owing to strong preferred orientation of the electrodes. The result indicates that the electrodes of  $\text{NbS}_2$  and  $\text{NaNbS}_2$  keep the same  $P6_3/mmc$  space group of  $\text{Na}_{0.5}\text{NbS}_2$ . An  $R3m$  structure of  $\text{NbS}_2$  does not fit the XRD pattern, so the possibility of a phase change to the  $R3m$  space group during charge is excluded.

Besides the electrode X-ray analysis for  $x = 0, 0.5$ , and  $1$ , powder X-ray experiments for the series of  $\text{Na}_x\text{NbS}_2$  ( $0.5 \leq x \leq 1.0$ ) were also performed, Figure 3, to check for a possible

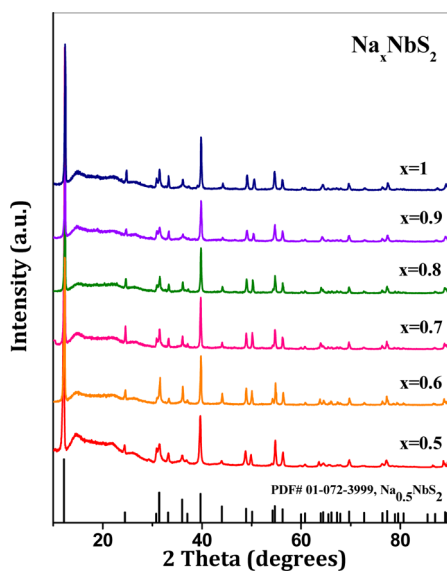


Figure 3. Powder XRD patterns of  $\text{Na}_x\text{NbS}_2$  ( $0.5 \leq x \leq 1.0$ ).

structural change near  $x = 0.75$ . The broad peak from  $15^\circ$  to  $21^\circ$  is ascribed to the amorphous polyimide film for sample sealing from moisture and oxygen. The patterns match well to the standard JCPDS reference card, and we could not see any phase changes or new phase evolution in this composition range. Figure 4 presents the lattice parameters calculated from XRD patterns shown in Figure 3. The  $c$ -axis of the unit cell decreases while the  $a$ -axis increases, which is generally the same trend as reported in Omloo et al.'s work in 1970.<sup>10</sup> However, one difference is that, at  $x \geq 0.7$  in  $\text{Na}_x\text{NbS}_2$ , the present data keep changing with  $x$  while the previous data show little change. In the past work, the quartz tube used was described as severely attacked by excess sodium, so the reaction between quartz and sodium must have reduced the net sodium content in the reactants and, hence, produced less change in the lattice parameters. In this work, double layers of carbon were coated on the inside of the quartz tube and 3 wt % excess  $\text{Na}_2\text{S}$  was added to make sure the designed sodium content will be inserted into the structure. The global trend explains well the sloping voltage curve in the composition range of  $0.5 < x < 0.75$  in  $\text{Na}_x\text{NbS}_2$ . However, the X-ray patterns and the lattice parameters do not explain well the relatively flat voltage curve at  $0.75 < x < 1.0$  in  $\text{Na}_x\text{NbS}_2$ . No secondary phase was observable in that compositional range, and the lattice parameter change is linear, indicating a solid solution. Again,

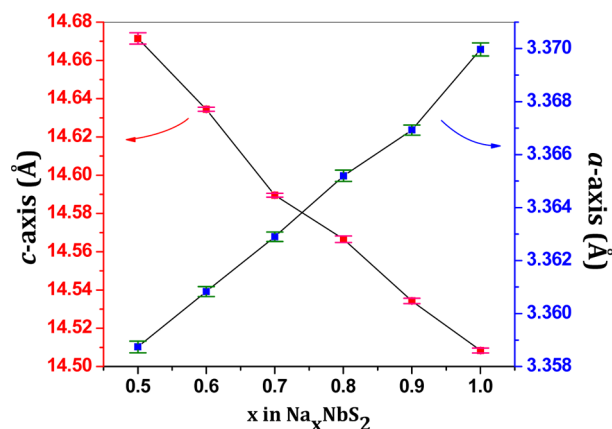


Figure 4. Unit-cell parameters of  $a$ - and  $c$ -axes calculated from the powder XRD patterns of  $\text{Na}_x\text{NbS}_2$  samples in  $P6_3/mmc$  space group ( $a = b \neq c$ ).

our calculations (described next) help to explain the electrochemical reactions. One final note is that, unfortunately, when the sodium content is less than 0.4 in  $\text{Na}_x\text{NbS}_2$ , the patterns become less crystalline with some broad peaks that did not match any JCPDS database. In Omloo et al.'s paper, they also could not get the cell parameters for  $x < 0.4$  in  $\text{Na}_x\text{NbS}_2$  and reported that the products contained  $\text{NbS}_2$ .

The galvanostatic charge/discharge cycle performance of  $\text{Na}_x\text{NbS}_2$  at  $C/20$  and  $C/10$  rates is presented in Figure 5. At

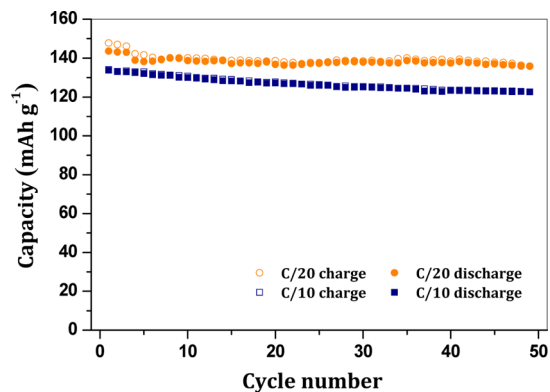
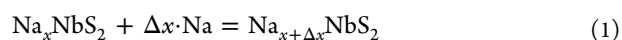


Figure 5. Charge/discharge cycle performance of  $\text{Na}_x\text{NbS}_2$  at  $C/20$  and  $C/10$  rates in the voltage range between 3.0 and 1.0 V at room temperature.

$C/20$  rate, the coin cell has a high discharge capacity:  $143.6 \text{ mAh g}^{-1}$  at the beginning, and keeps 94.6% ( $135.8 \text{ mAh g}^{-1}$ ) of the original capacity after 50 cycles with a Coulombic efficiency of 99.6%. If the current density is increased to  $C/10$ , the initial capacity,  $133.7 \text{ mAh g}^{-1}$ , becomes  $122.6 \text{ mAh g}^{-1}$  after 50 cycles (91.7% capacity retention). Even though the Na/vacancy ordering and the gliding of the  $\text{NbS}_2$  slabs are expected during charge/discharge, the cycle performance is impressive. The weakly bound  $\text{NbS}_2$  layers with the van der Waals bonding may give the good reversibility for the electrochemical structural changes.

In order to understand the electrochemical reaction, DFT calculations were performed. The Na binding energy is calculated as the reaction energy of the following equation,



and specifically as

$$E_{\text{bind}}(x) = \frac{E(\text{Na}_{x+\Delta x}\text{NbS}_2) - E(\text{Na}_x\text{NbS}_2) - \Delta x \cdot E(\text{Na})}{\Delta x} \quad (2)$$

We first determined the most probable Na site as Na is initially intercalated into the gallery space. A dilute Na intercalation case is simulated with  $x = 1$  in a  $\text{Na}_x\text{Nb}_{32}\text{S}_{64}$  supercell (a chemical composition of  $\text{Na}_{0.03}\text{NbS}_2$ ). Figure 6a shows two possible Na

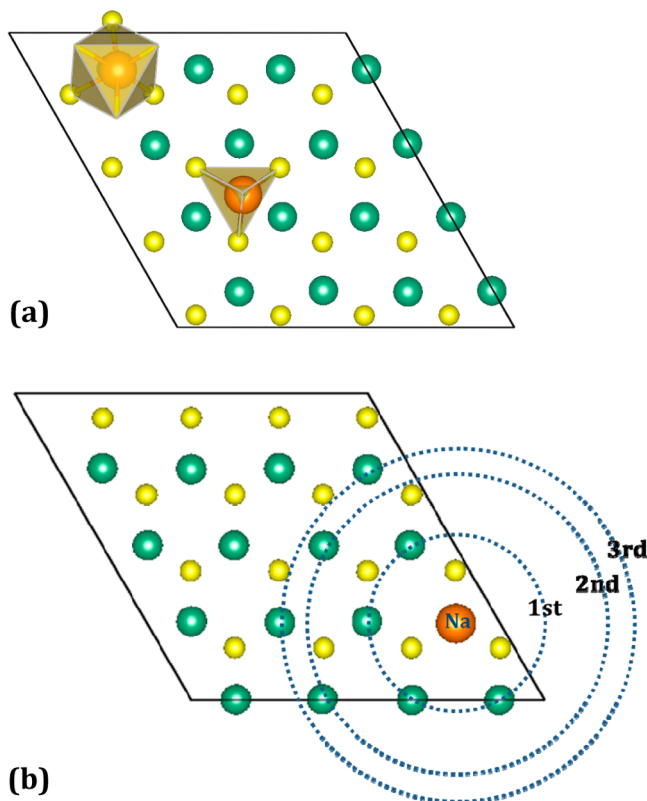


**Figure 6.** (a) Two possible Na sites in the gallery space; the first site is on top of a Nb, and the other is in the middle of a Nb triangle. (b) The Na positions in the first, second, and third nearest neighbors from a Na octahedral site.

sites; the first site is on top of a Nb atom, and the other is in a hollow in the middle of a Nb triangle. The top site is an octahedral configuration while the hollow site gives a tetrahedral environment. The Na binding energies with respect to Na metal are  $-2.71$  eV for the octahedral site and  $-2.56$  eV for the tetrahedral site. The octahedral site is favorable for intercalated Na by ca.  $0.15$  eV. Moreover, the calculated Na binding energy is very close to the experimental Na intercalation voltage in the  $\text{NbS}_2$  host (see Figure 1). One more notable fact is that, after putting Na in the octahedral site of the empty gallery space of the  $\text{Nb}_{32}\text{S}_{64}$  supercell, the relaxed unit-cell lattice parameter  $c$  is increased from  $12.81$  Å to  $13.56$  Å. Such a significant increase in the  $c$ -axis, together with the dilute Na concentration in the layer, could be an origin of the chemical inhomogeneity of  $\text{Na}_x\text{NbS}_2$  ( $0 < x < 0.4$ ) during the synthesis since, unlike the computational environment, the experimental condition cannot be ideally homogeneous in the precursor mixture.

Next, the intralayer interaction between the first Na in the octahedral site and the second Na is determined. The second

Na could be located at the first, second, and third nearest neighbor octahedral sites as shown in Figure 6b. In each case, the Na binding energies for the second Na are calculated to be  $-2.61$ ,  $-2.73$ , and  $-2.76$  eV, respectively. The first nearest neighbor site is less stable than more distant neighbors owing to the  $\text{Na}^+-\text{Na}^+$  electrostatic repulsion. However, it is interesting that the second and the third nearest neighbor sites increase Na binding. The reason for the enhanced Na stability is likely due to sharing of negative image charges between  $\text{Na}^+$  ions, as is understood in  $\text{LiFePO}_4$ .<sup>17</sup>

The interlayer Na interaction is also calculated between the first  $\text{Na}^+$  ion (Na1) and second  $\text{Na}^+$  ions (assigned as Na2a and Na2b) in the adjacent layer. Na2a is directly below the Na1 site and Na2b is the first nearest neighbor of the Na2a. The Na binding energies of Na2a and Na2b are  $-2.67$  and  $-2.66$  eV, respectively. Therefore,  $\text{Na}^+-\text{Na}^+$  interactions across the  $\text{NbS}_2$  slab are small regardless of the  $\text{Na}^+$  positions in this material. From the analysis, it is understood that the intralayer  $\text{Na}^+-\text{Na}^+$  interaction is important for the Na intercalation and the interlayer interaction has minimal effect on the Na binding energy.

On the basis of the Na-binding-energy analysis, we tried to find the global minimum structure of the material at different  $\text{Na}^+$ -ion intercalation stages in order to understand better the charge/discharge curve. A  $\text{Nb}_{32}\text{S}_{64}$  supercell containing  $4 \times 4 \times 2$  unit cells was used as a host structure. The minima-hopping method as implemented in ASE (Atomistic Simulation Environment) was first used for the Na half-filled composition,  $\text{Na}_{16}\text{Nb}_{32}\text{S}_{64}$ .<sup>18</sup> A glide between two  $\text{NbS}_2$  layers was observed. The glided structure is another host structure with only one type of  $\text{Na}^+$ -ion position, which is on top of one layer of Nb and in the hollow of the other layer of Nb, and the coordination number is still six, but in a trigonal prismatic geometry. To save computation time, basin-hopping was then performed separately on both the glided and not-glided host structures, with Na-vacancy swapping moves, to try to find the global minimum for the Na arrangement at different Na concentrations. The entire Na intercalation range was simulated for structures with 4, 8, 12, 14, 16, 20, 24, and 28 Na atoms in the supercell.

The formation energy of  $(\text{NaNbS}_2)_x(\text{NbS}_2)_{1-x}$  was calculated with respect to the not-glided  $\text{NaNbS}_2$  and  $\text{NbS}_2$  as

$$\begin{aligned} E_{\text{form}}(x) &= E((\text{NaNbS}_2)_x(\text{NbS}_2)_{1-x}) - x \cdot E(\text{NaNbS}_2) \\ &\quad - (1-x) \cdot E(\text{NbS}_2) \\ &= E(\text{Na}_x\text{NbS}_2) - x \cdot E(\text{NaNbS}_2) \\ &\quad - (1-x) \cdot E(\text{NbS}_2) \end{aligned} \quad (3)$$

Only the global minima are shown in the convex hull plot in Figure 7a. The slope of the hull is calculated as

$$\frac{\Delta E_{\text{form}}(x)}{\Delta x} = \frac{E(\text{Na}_{x+\Delta x}\text{NbS}_2) - E(\text{Na}_x\text{NbS}_2) - \Delta x \cdot E(\text{NaNbS}_2) + \Delta x \cdot E(\text{NbS}_2)}{\Delta x} \quad (4)$$

Compared with eq 2, the difference between the slope and the binding energy is a constant, which is the average Na binding energy over all the compositions and is independent of  $x$ ,

$$E_{\text{bind}} - \frac{\Delta E_{\text{form}}}{\Delta x} = E(\text{NaNbS}_2) - E(\text{NbS}_2) - E(\text{Na}) \quad (5)$$

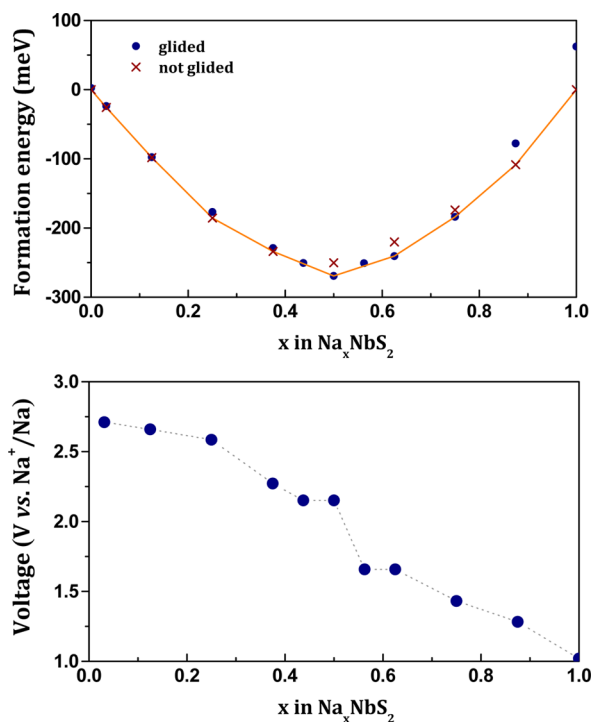


**Figure 7.** (a) Formation energy of  $(\text{NaNbS}_2)_x(\text{NbS}_2)_{1-x}$ , that is,  $\text{Na}_x\text{NbS}_2$ , with respect to the nonglided  $\text{NaNbS}_2$  and  $\text{NbS}_2$ . Only the lowest energy values at each concentration are shown for clarity. (b) Voltage calculated from the points on the convex hull.

The calculated voltage, shown in Figure 7b, captures the trend of the experimental charging/discharging curve, especially the voltage drop at  $x = 0.5$ . As Na concentration increases, Na atoms tend to disperse as uniformly as possible to reduce electrostatic repulsion. After the Na composition exceeds 0.5, the repulsive forces cannot be reduced further by Na rearrangement, so the binding-energy and voltage drop sharply. In compositions with  $x \leq 0.5$ , Na can disperse on next-neighbor sites to reduce the  $\text{Na}^+-\text{Na}^+$  repulsion.

As can be seen from Figure 7a, if the Na concentration is below 0.4, the differences between glided and not-glided structures are tiny, and the material can be a mixture of these two; from 0.4 to 0.8, the glided structures are energetically favorable; above 0.8, the not-glided structures are more stable. Experimental results in a previous report have confirmed that

$\text{Na}_{0.5}\text{NbS}_2$  is a glided structure although the Na ordering in this work was unsolved.<sup>11</sup>

Structures of  $\text{Na}_{0.5}\text{NbS}_2$  are compared in Figure 8. In the not-glided host structure, Na arranges in a zigzag way, similar to Li in  $\text{Li}_{0.5}\text{CoO}_2$ . The tetrahedral site is prohibited due to an energy rise from the coordination number drop. In the glided host structure, every other Na in the zigzag can move to its nearest neighbor site without any coordination number change, as the arrow indicates in Figure 8. The energy is further decreased by 19 meV per  $\text{Na}_{0.5}\text{NbS}_2$ . A similar Na ordering in the  $\text{VO}_2$  layered structure has been observed in a recent report.<sup>19</sup>

More configurations on the hull plot, displayed in Figure 9, give valuable information on the Na intercalation behavior. At low Na concentration, including  $\text{Na}_{0.125}\text{NbS}_2$  (not shown) and  $\text{Na}_{0.25}\text{NbS}_2$ , Na tends to have its neighbor Na at the third and then the second nearest neighbor sites, which is the same result found in the intraplane  $\text{Na}^+-\text{Na}^+$  interaction calculations. For  $\text{Na}_{0.375}\text{NbS}_2$ , only Na dimers are formed. In the  $\text{Na}_{0.5}\text{NbS}_2$  material, each Na connects to two other Na, and in  $\text{Na}_{0.625}\text{NbS}_2$  some Na connect to three other Na. The maximum connection from one Na to others increases to five for  $\text{Na}_{0.75}\text{NbS}_2$ . (Note that  $\text{Na}_{0.75}\text{NbS}_2$  is an ordered structure.) The connection number,  $N_c$ , is a good order parameter to distinguish phases of Na configurations. The phase transition from  $N_c = 2$  to  $N_c = 3$  gives the dramatic voltage drop.

We have noticed that energies versus  $x$  for  $\text{Li}_x\text{CoO}_2$  have a similar convex hull, but no sharp voltage drop has been observed experimentally.<sup>20,21</sup> We attribute this difference to the relatively high barrier for Li diffusion in the host structure (decreases from 600 to 200 meV as Li concentration increases), which makes it dynamically hard for the system to reach the global minimum while the Na diffusion barrier in the glided structure calculated with the climbing-nudged-elastic band method is only 77 meV in the dilute limit.<sup>22–24</sup>

#### 4. CONCLUSION

$\text{Na}_x\text{NbS}_2$  ( $0 \leq x \leq 1$ , space group =  $P6_3/mmc$ ) was studied as an electrode material for a Na-ion battery. The charge/discharge voltage profile shows a high specific capacity of  $143.6 \text{ mAh g}^{-1}$  with a signature of Na/vacancy ordering at  $x = 0.5$ . XRD analysis on the  $\text{Na}_x\text{NbS}_2$  electrodes and powders indicates no space group change during Na-intercalation. DFT calculations suggest possible atomic structures of  $\text{Na}_x\text{NbS}_2$ , including the Na/vacancy ordering at  $\text{Na}_{0.5}\text{NbS}_2$ . It is found that a gliding of  $\text{NbS}_2$  slabs is energetically favorable at  $0.5 \leq x$

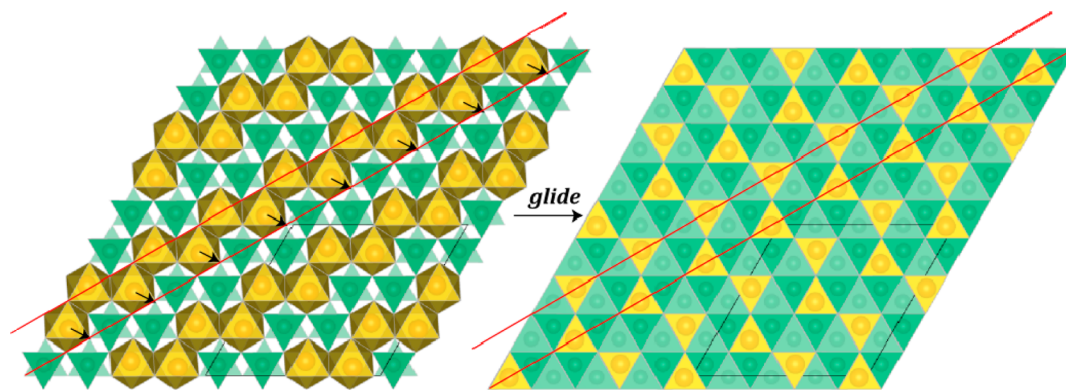


**Figure 8.** Comparison of nonglided and glided structures at  $\text{Na}_{0.5}\text{NbS}_2$ . Na atoms are yellow, Nb atoms are green, and S atoms are at the vertices. Atoms in lighter color are one layer beneath. Arrows show how Na redistributes to disperse more uniformly from left to right.

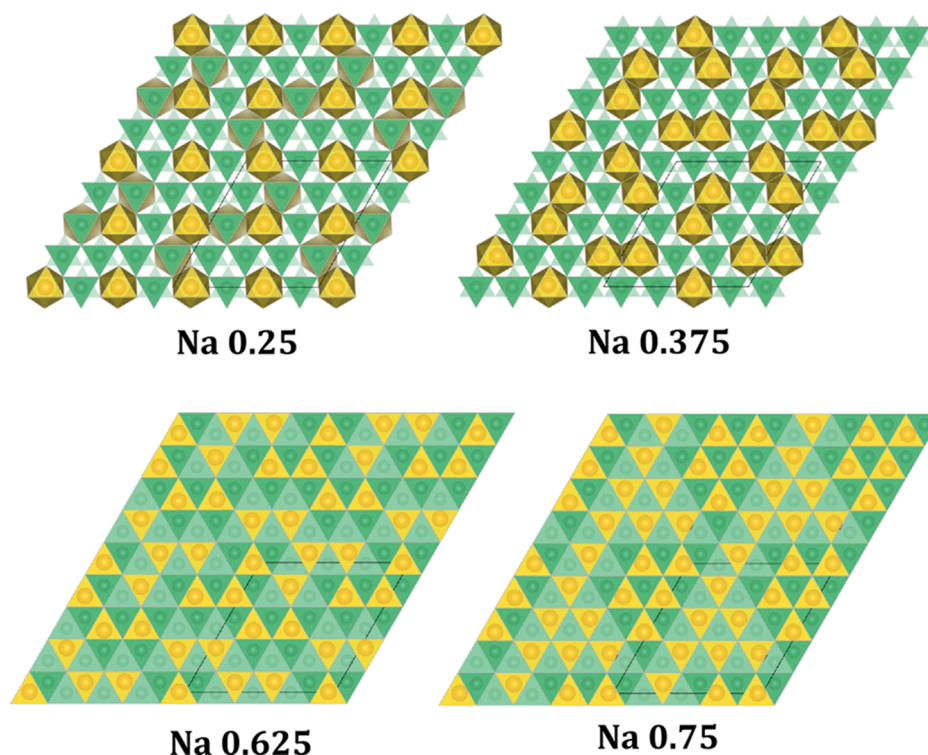


**Figure 9.** Structures on the convex hull. For  $\text{Na}_{0.25}\text{NbS}_2$ , the Na arrangement in the layer beneath is rotated by  $60^\circ$ ; for all the rest, the Na structure in each layer is the same.

$\leq 0.75$ . Overall the calculated voltage profile qualitatively agrees with the experimental results. The conclusion we want to emphasize is that not only the oxidation states of transition-metal cations but also the Na/vacancy arrangement play an important role in determining the voltage of the cathode. In  $\text{NaNbS}_2$ , the voltage varies by more than 1 V solely due to the  $\text{Na}^+ - \text{Na}^+$  interaction.  $\text{Na}_x\text{NbS}_2$  shows good cyclic performance and impressive Coulombic efficiencies suitable for a Na-ion battery, but the voltage profile is not suitable.

## ■ ASSOCIATED CONTENT

### 📄 Supporting Information

Galvanostatic Li-intercalation behavior of  $2\text{H-Li}_x\text{NbS}_2$ , 3D illustration of the most possible Na/vacancy ordering structure, and calculated lattice parameters of  $\text{Na}_x\text{NbS}_2$ . This material is available free of charge via the Internet at <http://pubs.acs.org>.

## ■ AUTHOR INFORMATION

### Corresponding Author

\*E-mail: [jgoodenough@mail.utexas.edu](mailto:jgoodenough@mail.utexas.edu).

### Author Contributions

<sup>†</sup>Y.L. and K.-S.P. contributed equally to this work.

### Notes

The authors declare no competing financial interest.

## ■ ACKNOWLEDGMENTS

This work was supported by the Robert A. Welch Foundation, Grant No. F-1066. Y.L. thanks the China Scholarship Council for supporting her stay at the University of Texas at Austin and also the financial support of NNSFC-NSFGP (Grant No. U1134002) and NSFGP (Grant No. 10351063101000001). The DFT calculations were supported as part of the program “Understanding Charge separation and Transfer at Interfaces in

Energy Materials (EFRC:CST)”, an Energy Frontier Research Center funded by the U.S. Department of Energy, Office of Science, Office of Basic Energy Sciences, under Award No. DE-SC0001091. Computational resources were provided by the Texas Advanced Computer Center.

## ■ REFERENCES

- (1) Goodenough, J. B.; Kim, Y. *Chem. Mater.* **2009**, *22*, 587.
- (2) Berthelot, R.; Carlier, D.; Delmas, C. *Nat. Mater.* **2011**, *10*, 74.
- (3) Yabuuchi, N.; Kajiyama, M.; Iwatate, J.; Nishikawa, H.; Hitomi, S.; Okuyama, R.; Usui, R.; Yamada, Y.; Komaba, S. *Nat. Mater.* **2012**, *11*, 512.
- (4) Komaba, S.; Yabuuchi, N.; Nakayama, T.; Ogata, A.; Ishikawa, T.; Nakai, I. *Inorg. Chem.* **2012**, *51*, 6211.
- (5) Komaba, S.; Takei, C.; Nakayama, T.; Ogata, A.; Yabuuchi, N. *Electrochem. Commun.* **2010**, *12*, 355.
- (6) Didier, C.; Guignard, M.; Denage, C.; Szajwaj, O.; Ito, S.; Saadoun, I.; Darriet, J.; Delmas, C. *Electrochem. Solid-State Lett.* **2011**, *14*, A75.
- (7) Moreau, P.; Guyomard, D.; Gaubicher, J.; Boucher, F. *Chem. Mater.* **2010**, *22*, 4126.
- (8) Plashnitsa, L. S.; Kobayashi, E.; Noguchi, Y.; Okada, S.; Yamaki, J.-I. *J. Electrochem. Soc.* **2010**, *157*, A536.
- (9) Jellinek, F.; Brauer, G.; Müller, H. *Nature* **1960**, *185*, 376.
- (10) Omloo, W. P. F. A. M.; Jellinek, F. *J. Less-Common Met.* **1970**, *20*, 121.
- (11) Salyer, P. A.; Barker, M. G.; Blake, A. J.; Gregory, D. H.; Weston, D. P.; Wilson, C. *J. Mater. Chem.* **2003**, *13*, 175.
- (12) Kohn, W.; Sham, L. J. *Phys. Rev.* **1965**, *140*, A1133.
- (13) Kohn, W.; Becke, A. D.; Parr, R. G. *J. Phys. Chem.* **1996**, *100*, 12974.
- (14) Perdew, J. P.; Wang, Y. *Phys. Rev. B* **1992**, *45*, 13244.
- (15) Wales, D. J.; Doye, J. P. K. *J. Phys. Chem. A* **1997**, *101*, 5111.
- (16) Dahn, D. C.; Carolan, J. F.; Haering, R. R. *Phys. Rev. B* **1986**, *33*, 5214.

- (17) Park, K.-S.; Xiao, P.; Kim, S. Y.; Dylla, A.; Choi, Y. M.; Henkelman, G.; Stevenson, K. J.; Goodenough, J. B. *Chem. Mater.* **2012**, *24*, 3212.
- (18) Goedecker, S. J. *Chem. Phys.* **2004**, *120*, 9911.
- (19) Guignard, M.; Didier, C.; Darriet, J.; Bordet, P.; Elkaïm, E.; Delmas, C. *Nat. Mater.* **2013**, *12*, 74.
- (20) Van der Ven, A.; Aydinol, M. K.; Ceder, G. *Phys. Rev. B* **1998**, *58*, 2975.
- (21) Reimers, J. N.; Dahn, J. R. *J. Electrochem. Soc.* **1992**, *139*, 2091.
- (22) Van der Ven, A.; Ceder, G. *J. Power Sources* **2001**, *97–98*, 529.
- (23) Henkelman, G.; Jónsson, H. *J. Chem. Phys.* **2000**, *113* (22), 9978.
- (24) Henkelman, G.; Jónsson, H. *J. Chem. Phys.* **2000**, *113* (22), 9901.